Enhanced removal of Co(II) and Ni(II) from high-salinity aqueous solution using reductive self-assembly of three-dimensional magnetic fungal hyphal/graphene oxide nanofibers

Runhua Chen [a], Yuying Cheng [a], Ping Wang [a,*], Qingwei Wang [c], Si Wan [d,e], Shunhong Huang [a], Rongkui Su [a], Yuxia Song [a], Yangyang Wang [b,*]

[a] College of Environmental Science and Engineering, Central South University of Forestry and Technology, Changsha 410007, China
[b] National Demonstration Center for Environmental and Planning, College of Environment & Planning, Henan University, Kaifeng 475004, China
[c] School of Metallurgy and Environment, Central South University, Changsha 410083, China
[d] Hunan Research Institute for Nonferrous Metals, Changsha 410100, China
[e] Faculty of Environmental Science and Engineering, Kunming University of Science and Technology, Kunming 650500, China

HIGHLIGHTS

- The adsorbent (MFHGs) exhibited a high capture capacity for Co(II) and Ni(II).
- MFHGs exhibited fast separation performance and denser sediment.
- MFHGs enhanced the stability and reusability of graphene oxide nanosheets.
- A reactor (CFRR) was designed for Co and Ni recovery from high-salinity aqueous solution.
- CFRR presented a satisfactory removal efficiency and regeneration performance.

GRAPHICAL ABSTRACT
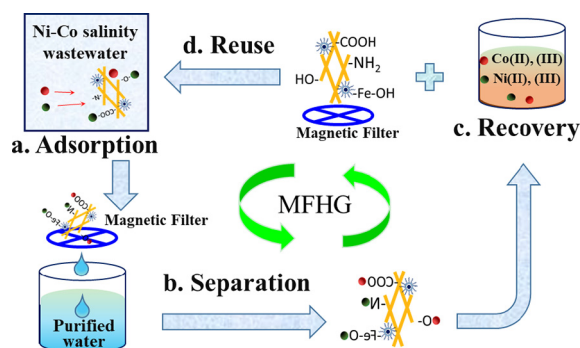
ABSTRACT

Layer-structured graphene oxide excellent carrier for modifications; however, its poor recoverability and stability preclude its application in wastewater treatment fields. Herein, three-dimensional magnetic fungal hyphal/graphene oxide nanofibers (MFHGs) were assembled by a reductive self-assembly (RSA) strategy for the efficient capture of Co(II) and Ni(II) from high-salinity aqueous solution. The RSA strategy is inexpensive, eco-friendly and easy to scale up. The obtained MFHGs enhanced the dispersity and stability of graphene oxide and exhibited excellent magnetization and large coercivity, leading to satisfactory solid-liquid separation performance and denser sediment. The results of batch removal experiments showed that the maximum removal capacity of MFHGs for Ni(II) and Co(II) was 97.44 and 104.34 mg/g, respectively, in 2 g/L Na_2SO_4 aqueous solution with a pH of 6.0 at 323 K, and the effects of initial pH and ionic strength on Co(II) and Ni(II) removal were explored. Yield residue analysis indicated that the high porosity and oxygen-containing functional groups of MFHGs remarkably improved their Co(II)- and Ni(II)-removal capacities. According to the analysis, hydroxyl groups and amine groups participated in the chemical reaction of Co(II) and Ni(II) removal, and cation-exchange chemical adsorption was dominant during the Co(II)- and Ni(II)-removal process. Based on the attributes of MFHGs, a continuous-flow recycle reactor

* Corresponding authors.
  E-mail addresses: wangyangyangxyz@163.com (Y. Wang), csfuwp@163.com (P. Wang).

(CFRR) was proposed for emergency aqueous solution treatment and exhibited satisfactory removal efficiency and regeneration performance. The combination of MFHGs and the proposed CFRR is a promising water treatment strategy for rapid treatment applications.

1. Introduction

The development of the battery industry has led to the generation of a large amount of wastewater with high salt content, extreme solution pH and various heavy metals; this wastewater has become an urgent environmental problem worldwide (Lee et al., 2016; Zhao et al., 2020). Co(II) and Ni(II) are the main heavy metals in battery-industry wastewater, and they are ranked among the most toxic heavy metals due to their extreme biological toxicity (Fang et al., 2018). Co(II) and Ni(II) cause serious symptoms and diseases such as nausea, vomiting, chest pain, inflammation, neurasthenia, cancer, teratogenesis, and mutagenesis (Lapwanit et al., 2016; Wang et al., 2021). The effluent discharge concentration limits for Co(II) and Ni(II) in general areas in China are 1.0 and 0.5 mg/L (Wang et al., 2019), respectively. To reduce pollutant emissions of Co(II) and Ni(II), various methods, such as chemical precipitation, electrochemical separation, membrane separation, ion exchange, electrolysis, and adsorption, have been used to the remove Co(II) and Ni(II) from wastewater (Liu et al., 2019). Among these methods, adsorption is the generally considered to be cost-effective, simple and efficient. Some studies have reported the adsorption of Co(II) and Ni(II) by biochar, such as straw, peanut shells and sewage sludge biochar (Bogusz et al., 2017; Vithanage et al., 2020). However, the adsorption capacity of biochar for Co(II) and Ni(II) was too low. Moreover, high-salt-content Co(II) and Ni(II) effluents with high solution pH lead to complex competition among adsorption, the common-ion effect, and the salting-out effect. Thus, the development of cost-effective adsorbents and a corresponding strategy for Co(II) and Ni(II) adsorption remains a challenge.

Fungal hyphal (FH) fiber is a sustainable biological resource that can be obtained from waste or cultivated on a large scale (Jones et al., 2019). Due to its efficient and low-cost use in wastewater treatment, it has attracted increasing attention in adsorptive applications (Yi et al., 2020). However, FH fibers with poor porosity result in a relatively low adsorption capacity, which limits their large-scale application. In recent years, the development of FH nanomaterials has been a research hotspot. Recent studies have reported that the assembly of nanomaterials via the growth of FH (Chen et al., 2020; Zhu et al., 2019) is simple, efficient and extremely feasible. However, the metabolite impurities in the products prepared by this method may need to be cleaned many times (Zhang et al., 2021). Post-modifying FH fibers increases the total profit from physical/chemical activation processes by providing an FH product with a higher porosity or greater density of surface functional groups (Huang et al., 2020). Thus, several post-modification methods, including carbonization (Lei et al., 2019) and chemical oxide or organic modification (Cárdenas-González et al., 2017), have been developed to improve the FH fiber performance. However, carbonization or thermochemical modification requires high temperatures, long cycle times and extra chemical agents, making it uneconomical and resulting in high production costs and remarkable secondary pollution. It is necessary to develop efficient post-engineering strategies to improve the performance of hyphal fibers without inducing high costs, long cycle times and serious secondary pollution.

There are hundreds of companies all over the world that produce various types of graphene oxide and its derivatives with very different properties (Kauling et al., 2018); in addition, layer-structured graphene oxide has attracted wide attention in many new applications because of its unique structure and outstanding physical and chemical properties.

Graphene oxide exhibits a strong adsorption capacity for contaminants. Thus, the amendment of graphene oxide via organic chemicals or high concentrations of oxidants (e.g., HNO_3, NaOH, H_2O_2, or their mixtures) for wastewater purification has gained considerable attention and possesses satisfactory removal performance for various of contaminants. However, this strategy is difficult to be scaled up for practical production because of the associated low efficiency and high cost. In addition, organic chemical modification processes can generate a large amount of organic wastewater, which would also limit their practical application (Zhang et al., 2020).

Reductive self-assembly (RSA) processes for the magnetization and graphene oxide grafting treatment of hyphal fibers are conducted in a mild aqueous solution. Compared with thermochemical modification (Fan et al., 2020; Rwiza et al., 2018), RSA has been employed in the preparation of various composite nanomaterials due to its normal pressure and temperature and consumption of less energy while providing a greater product yield (Jiao et al., 2015; Liang et al., 2015). In particular, compared with thermochemical modification, RSA should be a greener approach that enables satisfactory magnetic recovery efficiency and high product yield without involving the addition of organic and oxidizing chemical agents. RSA might be a simple and convenient strategy to be scaled up for the commercial production of hyphal fiber adsorbents. Thus, it might enhance the Co(II) and Ni(II) adsorption performance by hyphal fiber and reveal the adsorption mechanism between the dominant organic group receptor and heavy metals in solutions with extremely high salt contents. However, little is known about the effects of RSA on the surface engineering of hyphal fibers and the subsequent effects on Co(II) and Ni(II) adsorption performance. Therefore, it would be very valuable to identify strategies that are feasible, eco-friendly, and efficient in their capacity for Co(II) and Ni(II) wastewater treatment.

In this work, three-dimensional (3D)-structured magnetic fungal hyphal/graphene oxide nanofibers (MFHGs) with high specific surface areas and multi-groups were synthesized by RSA methods under mild conditions. Based on the attributes of the MFHGs, a novel continuous-flow recycle reactor (CFRR) was designed for the high-efficiency treatment of Co(II) and Ni(II) from high-salinity aqueous solutions. The removal efficiency of Co(II) and Ni(II), residue separation efficiency, regeneration and reusability of MFHGs were discussed in detail. In addition, the adsorption kinetics and isotherms of reductive self-assembled MFHGs toward Co(II) and Ni(II) were analyzed to explore the potential adsorption mechanism. Furthermore, energy gaps (ΔE) and stable configuration of heavy-metal complexes in yield residue were calculated by density functional theory (DFT) to evaluate the MFHGs and the RSA engineering strategy. This research highlights the feasibility of the RSA strategy, the easy separation features of MFHGs and their practical application in a CFRR strategy for Co(II) and Ni(II) aqueous solutions.

2. Materials and methods

2.1. Materials

A freeze-dried strain tube of *Aspergillus niger* (ATCC 16404) was obtained from the General Microorganisms Collection and Management Center in Wuhan, China. The graphene oxide suspension (5 mg/mL in an aqueous solvent) was purchased from the Suzhou Tanfeng Graphene Technology Co., Ltd.; more information is detailed in supplementary material Fig. S1 and Table S1. A stock solution of Co(II) and Ni(II) was

prepared by dissolving nickel sulfate ($NiSO_4$) and cobalt sulfate ($CoSO_4$) in Milli-Q water. An appropriate amount of sodium sulfate (Na_2SO_4) was dissolved into the aforementioned stock solution to simulate actual wastewater. Green vitriol ($FeSO_4 \cdot 7H_2O$), sodium borohydride ($NaBH_4$), nickel sulfate ($NiSO_4$), cobalt sulfate ($CoSO_4$), sulfuric acid (H_2SO_4), sodium hydroxide ($NaOH$) and ethanol were all purchased from Sinopharm Chemical Reagent Co., Ltd. All chemicals were of analytical grade and were directly utilized after purchase, without further purification.

2.2. RSA of hyphal fibers

MFHGs were prepared by an RSA method. Briefly, *A. niger* was incubated in PDA liquid medium (potatoes 200 g/L, glucose 20 g/L, ddH_2O 1 L) to obtain mung-bean-sized FH spheres; the detailed procedure is provided in the supporting information. The FH spheres were inactivated by boiling and then crushed into a suspension of dispersed hyphal fibers. After repeated washing, 200 mL (80 g/L) of the dispersed hyphal fibers suspension was transferred to a reflux flask under 150 rpm mechanical stirring at 25 °C. However, 1 mL (5 mg/mL) of graphene oxide suspension was added to a tube, and then, 5 mL of 5% H_2O_2 aqueous solution was injected, followed by ultrasonic dispersion for 10 min before use. Then, 5 mL (1 g/L) of graphene oxide suspension was injected slowly under continuous stirring, followed by 30 min of self-assembly reaction under water shear force to form the FH/graphene oxide winding structure. Then, 50 mL of $FeSO_4$ acidified aqueous solution (100 g/L) was added to the flask under continuous stirring until the ferrous ions were well distributed; 50 mL of $NaBH_4$ solution (5 g/L) was gradually added dropwise under vigorous stirring, and the reaction was continued for another 30 min. The resulting residue was collected under a magnetic field and washed until the filtrate was clear. Finally, the obtained residue was further oxidized in a tube furnace under 80 °C natural air conditions to obtain MFHGs.

2.3. Batch experiments

Batch adsorption experiments were performed by adding 0.1 g of MFHGs to 100 mL of simulated aqueous solution containing Na_2SO_4 (2 g/L) and various concentrations of Co(II) and Ni(II). The initial pH of the solution was adjusted from 2.0 to 11.0 by adding negligible amounts of H_2SO_4 or NaOH (0.01–1.0 mol/L) solution, the Co(II) or Ni(II) initial concentration of the solutions was controlled in the range from 20 to 160 mg/L, and then the MFHG mixed suspensions were shaken on an orbital shaker at 100 rpm to reach adsorption equilibrium. Afterwards, the MFHG residue was directly separated from the

suspensions via their stronger magnetism. To evaluate the removal effects of MFHGs toward Co(II) and Ni(II), all residual concentrations of Co(II) and Ni(II) in aqueous solution were measured by inductive coupled plasma emission spectrometry (ICP; PerkinElmer 8300, Germany). The formula used to calculate the Co(II) and Ni(II) residual content and removal rate is detailed in supplementary material S1.2.

2.4. CFRR reactor

The practical application of water treatment agents is often realized through combination with engineering equipment. Based on the attributes of MFHGs, a laboratory-scale continuous flow recycle reactor (CFRR, diameter = 12 cm, height = 30 cm, total volume = 3.39 L) was used for purification of high-salinity Co(II) and Ni(II) aqueous solutions. The CFRR based on MFHGs is displayed in Fig. 1. It is a complete and portable water treatment system based on the MFHG agents. During the treatment, the magnetic MFHGs with rich porosity and organic functional groups were mixed as the adsorption carrier into the solution by continuous stirring. The initial MFHG concentration was set at 2.0 g/L. After reaction, the aqueous solution with mixed MFHGs (adsorbed) was transferred by peristaltic pump to the magnetic separator at a flow velocity of 0.9 mL/min. After magnetic separation, purified water and MFHGs (adsorbed) were produced. The treated water was discharged outside of the CFRR system, and the MFHGs (adsorbed) were collected for the activation. MFHGs (adsorbed) were activated by 5 mol/L hydrochloric acid to obtain MFHGs (activated), which could be reused in the CFRR directly. Hence, the waste after acid eluent should be recycled for heavy metals and acids by distillation; thus, volatile hydrochloric acid and nitric acid are more suitable for the recycling of valuable metals.

2.5. Characterization

The magnetic properties of the MFHGs were characterized by vibrating sample magnetometry (VSM; MPMS XL-7, USA). The morphological structure was characterized by scanning electron microscopy (SEM; Sigma HD, USA). Thermogravimetric and differential thermal analysis (TG-DTA; Netzsch Sta 2500, Germany) was carried out to measure the mass change in the samples at different temperatures and under different atmospheres to explore the thermal stability and composition of the samples. X-ray diffraction (XRD; Panalytical B.V., The Netherlands) patterns were collected to analyze the changes in crystallinity between the MFHGs and other samples. The surface functional groups of various samples were determined by Fourier transform infrared spectroscopy (FTIR; Thermo Scientific Nicolet iS5, USA). X-ray photoelectron spectroscopy (XPS; Thermo Scientific K-Alpha$^+$, USA) was employed to
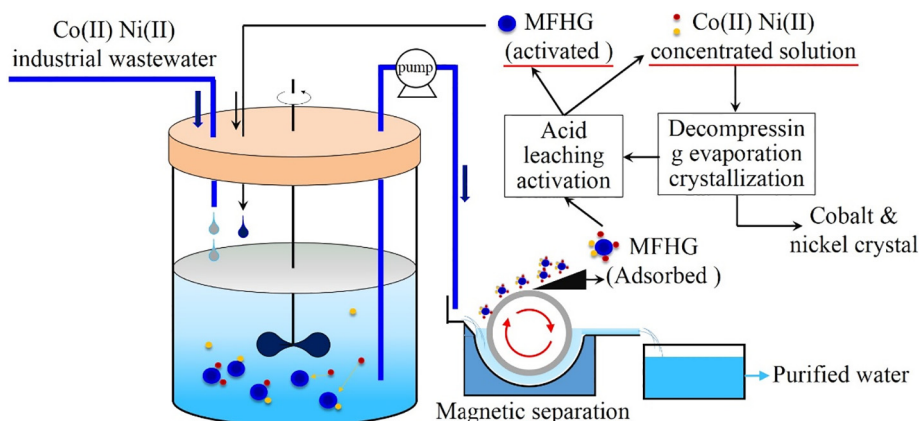

Fig. 1. The continuous flow recycle reactor (CFRR) of MFHGs for heavy-metal-containing wastewater.

analyze the relationship between functional group changes and the chelating forms of heavy metals. The specific surface area and the porous features were investigated by nitrogen isothermal adsorption/desorption measurements, and the specific surface area was calculated using the Brunauer-Emmett-Teller (BET) method at 77 K.

2.6. DFT calculation

The mechanism of Co(II) and Ni(II) adsorption onto the MFHGs was investigated by DFT calculations using Gauss 5.0, and the GaussView molecular visualization software was used to draw the initial structure and to visualize the results (Chen et al., 2019). The molecular structure of the heavy-metal derivative was optimized by spin-unrestricted-polarization DFT based on the generalized gradient approximation (GGA) with the Becke-Lee-Yang-Parr (BLYP) correlation energy function in the gas phase with the 6-311Gþþ (d,p) basis set and default SCF and geometrical convergence criteria. The information about delocalization of charge in the heavy-metal compound was provided through NBO analysis using the Gaussian NBO 3.1 program at the same DFT level with the POP═NBO keyword. The chemical stability of the heavy-metal compounds in the yield residue was evaluated in view of global reactivity descriptors and frontier orbital energies. All energy gaps (ΔE) were calculated according to the following equation:

$$\Delta E = E_{HOMO} - E_{LUMO} \tag{1}$$

where E_{HOMO} is the highest occupied molecular energy of the optimized models in the residue after adsorption, and E_{LUMO} is the lowest unoccupied molecular energy of the optimized models in the residue after adsorption.

3. Results and discussion

3.1. Characterization of MFHGs

MFHGs were prepared by the RSA method, and the synthesis of MFHGs is schematically illustrated in Fig. 2. Sponge-like FH/graphene oxide nanofibers were first obtained through a suitable aqueous liquid medium under rotating shock culture. The zeta potentials of FH and graphene oxide have low absolute values and opposite charges (Table S2). The electrostatic action under continuous water shear force should lead to polymerization cross-linking between the graphene oxide nanosheets and FH nanofibers, resulting in the formation of a sponge-like intertwined structure (Zhu et al., 2019). In the case of uniform magnetization, a special pre-adsorption and reductive strategy provided a satisfactory dispersion of the nanometer iron with an excellent pore structure, which is beneficial for heavy-metal removal. In addition, this strategy is simple, inexpensive and easy to scale up; it could enable the simultaneous synthesis of various cross-linked sponge-like structures with various functional groups for use in catalysis or interfacial reactions.

SEM was employed to observe the surface physical morphology of FH (Fig. 3a), FH@graphene oxide nanofibers (Fig. 3b) and the as-synthesized MFHGs (Fig. 3c and d). The FH were entangled and exhibited a reticulated structure, which resulted from the original filaments of the FH fibers. A range of membrane-like substances emerged on the surface of the FH nanowires after the polymerization process, and small graphene oxide nanosheets were formed with a particularly rough surface. This behavior might be attributable to the implantation pretreatment of graphene oxide nanosheets. As shown in Fig. 3c and d, the particles with a regular sphere-like shape and homogeneous size of 150–200 nm were evenly distributed on the surface of the MFHGs, which formed nanosized core-layer composites. The SEM results indicate that graphene oxide and iron were successfully attached to the surface of FH. In addition, the specific surface area and porosity of FH, FH@graphene oxide nanofibers and the MFHGs were characterized by the BET method. The specific surface areas of FH, FH@graphene oxide nanofibers and MFHGs were 59.47, 321.13 and 263.19 m^2/g, respectively. FH@graphene oxide nanofibers possessed a much greater surface area than the FH nanofibers, which can be explained by the multilayer of graphene oxide. However, the specific surface area of the MFHGs was slightly lower than that of FH@graphene oxide nanofibers, which is attributed to the weight of dispersed FeO$_x$ during the magnetization process (Qiu et al., 2020).

To reliably describe of the magnetic properties of MFHGs, the magnetic properties of FH, graphene oxide nanosheets and MFHGs were characterized and are presented in Fig. 3e. The saturation magnetization (Ms) value of the MFHG nanoparticles was 51.36 emu/g, whereas the graphene oxide nanosheets and FH exhibited no magnetism. The hysteresis loops indicate that MFHGs exhibited excellent magnetization with large coercivity and could be swiftly separated from the solution by a simple magnet (Fig. S2). This reveals that the MFHGs can be easily separated from solution because of their strong magnetization (Najafpoor et al., 2020).

The different bending and stretching vibrations of FH, FH@graphene oxide nanofibers, and MFHGs were investigated using laser FTIR spectroscopy. As shown in Fig. 3f, the spectrum of FH contains peaks at
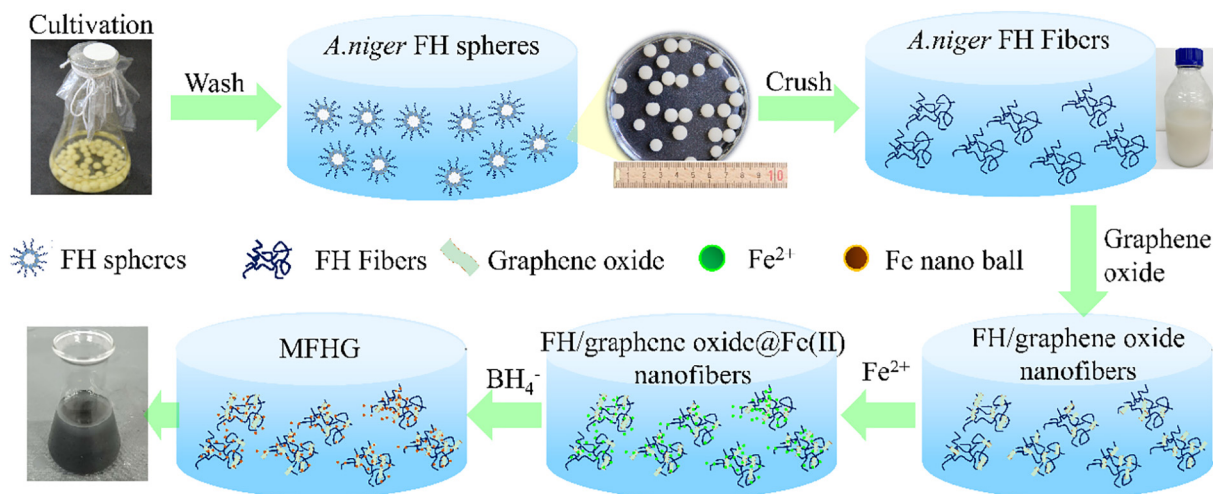

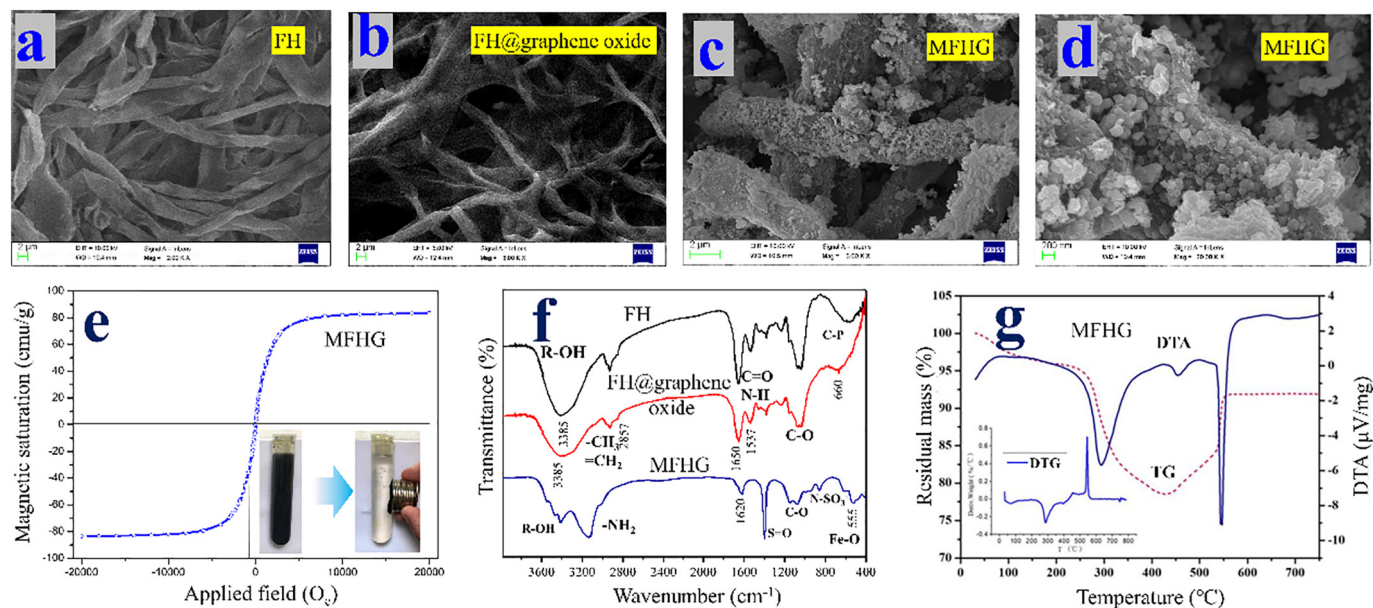**Fig. 2.** Synthesis process of MFHG.

Fig. 3. SEM images (a: FH, b: FH@graphene oxide, c and d: MFHGs). Magnetic hysteresis loops of MFHGs (e); FTIR spectra of FH, FH@graphene oxide and MFHGs (f), and TG-DTA thermogram of MFHGs (g).

3385 cm^{-1} (C-OH stretching), 2926 cm^{-1} (=CH$_2$-CH$_3$ stretching), 1650 cm^{-1} (C=O stretching), 1537 cm^{-1} (N—H stretching), 1380 cm^{-1} (S=O stretching), and 1075 cm^{-1} (C—O stretching) (Samuel et al., 2018; Yang et al., 2019). These signals correspond to protein and sporopollenin present on the surface of FH. The spectrum of FH@graphene oxide nanofibers is similar to that of FH, with some differences in peak intensity and position. The most important changes are the enhanced intensity and peak shifts at 660 cm^{-1} and 1075 cm^{-1}, indicating the enrichment of C—O groups on FH. We further inferred that the complexation of graphene oxide with FH increased the functional-group loading sites on FH. Moreover, the spectrum of MFHGs shows obvious changes in terms of peak shifts due to the modification of the iron ions and sulfate radicals. New peaks appeared at 555, 850 and 1387 cm^{-1}, which were attributed to the characteristic stretching vibrations of Fe—O, SO-OH and S=O (Kumar et al., 2020; Meteku et al., 2020), respectively. The appearance of these peaks indicates that sulfo and iron oxide groups were grafted successfully. In addition, the minor attenuation in intensity at 1620 and 1075 cm^{-1} is attributed to the involvement of C—O groups in ferrous binding. These changes can be explained by the formation of Fe-organic complexes with carboxyl and hydroxyl groups on the surface of the MFHGs (Velimirovic et al., 2018). These results show that MFHGs were successfully prepared and that the surface of the MFHGs is rich in functional groups (-OH, S=O, C—O, etc.).

TG and DTA measurements were carried out in an oxygen atmosphere to determine the thermal stability of the MFHGs. As shown in Fig. 3g, three significant changes are observed in the TG and DTA curves from 0 to 800 °C. First, the weight loss at 30–110 °C was attributed to the evaporation of physisorbed water and loosely bound water molecules. Second, the weight loss between 280.5 and 435.6 °C was attributed to the removal of organic groups (i.e., -OH, S=O, C—O, etc.) (Liu et al., 2016). Third, a wide endothermic peak at 545.6 °C is observed, and the weight value increased by 6.16%, which was attributed to structural changes in the ferrous metals, perhaps due to the conversion of amorphous iron phases into other crystal forms. In general, when the temperature is increased to approximately 260 °C, the weight loss is only 5%; in addition, the weight loss of the material over the entire heating process is not large, which proves that MFHGs have good thermal stability (Zhao et al., 2010).

3.2. Adsorption kinetics and isotherms

Adsorption kinetic experiments were carried out to investigate the removal mechanism of Co(II) and Ni(II) by MFHGs. Pseudo-first-order and pseudo-second-order kinetic models were used to fit the experimental data (Firdaous et al., 2017). The kinetic constants of Co(II) and Ni(II) removal by MFHGs are shown in Table S3. The pseudo-second-order kinetic models (Fig. 4c-d) show a better fit than the pseudo-first-order models (Fig. 4a-b), revealing that the rate of adsorption for absorbents should be dependent on the amount of active functional-group sites. Moreover, Co(II) and Ni(II) adsorption onto MFHGs could be limited by the chemical adsorption involving electron sharing and ion exchange between the active functional group sites and heavy-metal cations.

Fig. 4e and f show typical adsorption isotherms of Co(II) and Ni(II) interacting with MFHGs according to Langmuir and Freundlich adsorption isotherms, respectively. The values of the corresponding maximum adsorption capacity, q$_m$, are given in Table S4. Adsorption studies for Co(II) and Ni(II) were carried out at 293, 308 and 323 K for MFHGs. The removal amount of Co(II) and Ni(II) on MFHGs increased with increasing initial concentration and temperature. The maximum adsorption capacity of MFHGs at 293, 308 and 323 K was 76.11, 84.80, 97.44 mg/g for Ni(II) and 100.29, 104.21, 104.34 mg/g for Co(II), respectively. The removal behaviors of Co(II) and Ni(II) by MFHGs were better fit by the Langmuir model at 293, 308 and 323 K. We inferred that the reaction is characterized by uniform monolayer surface chemical adsorption. In addition, the removal capacity of MFHGs is compared with that of the same type of nano-adsorbent in Table 1 revealing that the MFHGs synthesized in this study have a satisfactory removal capacity.

3.3. Removal of Co(II) and Ni(II) from aqueous solutions

The initial pH affects the speciation of heavy-metal ions in solution as well as the surface charge of the adsorbent. The influence of pH on the removal of Co(II) and Ni(II) by MFHGs and graphene oxide nanosheets is presented in Fig. S3 a and b, respectively. The results show that the solution pH strongly affected Co(II) and Ni(II) removal. The removal capacity of MFHGs for Co(II) and Ni(II) reached approximately
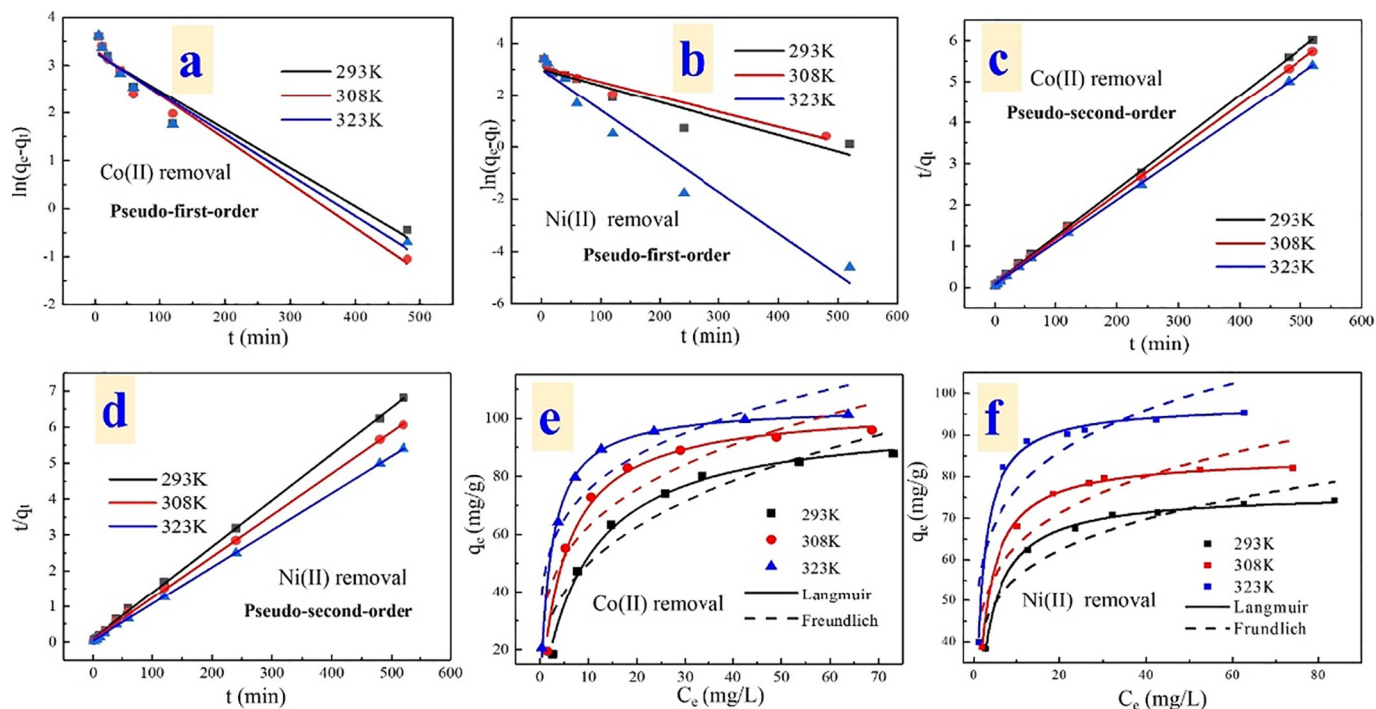
Fig. 4. Pseudo-first-order kinetic model of the uptake of Co(II) (a) and Ni(II) (b) by MFHGs. Pseudo-second-order kinetic model of the uptake of Co(II) (c) and Ni(II) (d) by MFHGs. Nonlinear fitting of equilibrium data to the Langmuir and Freundlich isotherms for the adsorption of Co(II) (e) and Ni(II) (f) onto MFHGs at various temperatures.

120 mg/g at pH 10.5 but was only 26.5 mg/g at pH 2.0. Accordingly, the relative distributions of Co(II) and Ni(II) species were calculated by Visual MINTEQ (ver. 3.0) (Sierra et al., 2017). Notably, the positively charged Co(II) and Ni(II) ions were the major species existing in acidic solution (Fig. S3 c and d). The removal of Co(II) and Ni(II) by MFHGs was favorable in alkaline solution. The zeta potential analysis results show that the surface of MFHG is negatively charged under alkaline conditions (Fig. S4), which might be attributable to electrostatic

interactions between the negatively charged surface and Co(II) and Ni (II) cations. The surface groups (COO⁻, O⁻, NH⁻, etc.) of MFHGs would be occupied by hydrogen ions at lower pH levels, which would adversely affect the removal capacity of Co(II) and Ni(II) at pH < 2.0. In addition, the removal capacities of Co(II) and Ni(II) by graphene oxide nanosheets were 60 mg/g or lower in the pH range from 2.0 to 8.0. When the pH of the solution was increased to pH 10.5, the maximum removal capacities of graphene oxide nanosheets for Co(II) and

Table 1
Comparison of the removal properties of MFHGs and other adsorbents for Co(II) or Ni(II).

Metal ion	Adsorbent	Aqueous condition	Removal capacity (mg/g)	References
Co(II)	Graphene oxide	Water aqueous (pH ~ 5)	88.98	(Chaabane et al., 2020)
	functionalized RGO	Water aqueous	41.2	(Zhang et al., 2018)
	Pyridine-based polymer: PAPY, M4195 and TP220	Acidic aqueous (pH ~ 2)	53.28, 40.19 and 56.63	(Zong et al., 2018)
	Spirulina sp. and activated charcoal	Leachate of lithium-ion batteries	95.9 and 50.3	(Peres et al., 2018)
	Magnetic phosphorylated chitosan composite (P-MCS)	Aqueous	46.1	(Yuan et al., 2020)
	Activated carbon from worn tires	Aqueous	90.09	(Abbasi et al., 2019)
	Metakaolin-based geopolymer	Aqueous	69.23	(Kara et al., 2018)
	Zeolite (NaA)	Terephthalic acid wastewater	56.2	(Lin et al., 2020)
	Pyrophyllite mine waste-based geopolymer	Aqueous	7.18	(Panda et al., 2018)
	Ligand-anchoring optical composite adsorbent (CpAD)	Aqueous	185.23	(Awual et al., 2020)
	MFHGs	Saline	104.34	This work
Ni(II)	Graphene oxide	Aqueous	39.0	(Zare-Dorabei et al., 2016)
	Graphene oxide	Aqueous (pH ~ 5)	105.0	(Chaabane et al., 2020)
	Pyridine-based polymer: PAPY, M4195 and TP220	Acidic aqueous (pH ~ 2)	87.10, 74.54 and 81.34	(Zong et al., 2018)
	Alginate and magadiite/di-(2-ethylhexyl) phosphoric acid	Aqueous	44.0	(Attar et al., 2019)
	Cattle manure (CM) and cattle manure biochar (CMB)	Aqueous	13.9 and 11.1	(Wang et al., 2020)
	CTAB-intercalated molybdenum disulfide nanosheets	Aqueous	88.3	(Cai et al., 2020)
	Ni(II)-IIPs	Aqueous	86.3	(Zhou et al., 2018)
	Silica-supported hydrophilic carbonaceous nanoparticles (SHNPs)	Aqueous	13.48	(Di Natale et al., 2020)
	Microwave-functionalized cellulose	Aqueous	72.80	(Chen et al., 2020)
	Magnetic anionic hydrogel (nFeMAH)	Aqueous	93.00	(Badsha et al., 2020)
	MFHGs	Saline	97.44	This work

Ni(II) increased to 68.15 mg/g and 58.79 mg/g, respectively, much lower than that achieved by MFHGs.

In the field of heavy-metal wastewater treatment and resource utilization, the rapid separation of suspended solid residue and supernatant is a very challenging technical problem (Hou et al., 2020). The separation performance and compactness of residues resulting from the removal of Co(II) and Ni(II) by MFHGs and traditional NaOH chemical precipitation processes are compared and illustrated in Fig. S5. The pH of the solution (25 mL) containing 20 mg/L Co(II) or Ni(II) was varied from 7.0 to 12.0, and the solution was cooled for 20 min after being thoroughly mixed at 25 °C. The results in Fig. S5 left show that the aqueous solution gradually became cloudy with increasing pH. However, precipitation was still difficult after 20 min (Fig. S5 left). As shown in Fig. S5 right, the separation capability improved rapidly with the addition of MFHGs compared with Fig. S5 left. In addition, the density of the MFHG residue increased significantly at pH 9, and the residue volume decreased dramatically. These results were attributed to colloidal destabilization between the hydroxide suspension and various organic groups on the surface of the long chains of MFHGs. These results reveal that MFHGs can greatly reduce the cost of separation processes and would be highly convenient for the treatment of large quantities of wastewater.

3.4. Adsorption mechanisms

FTIR was used to analyze the chemical bonds of the MFHGs before and after adsorption (Fig. 5a). MFHGs after Co(II) and Ni(II) adsorption showed similar surface functional groups compared with their pristine counterpart. However, various bands for MFHGs after adsorption, e.g., bands C-OH at 3385 cm^{-1} and C=O (N—H) at 1650 cm^{-1}, were slightly weakened or exhibited a slight shift. These results indicate that the aforementioned functional groups participated in the chemical reaction of Co(II) and Ni(II) adsorption. Moreover, after Co(II) and Ni(II) adsorption, a new heavy-metal group peak appeared at 530 cm^{-1} and the S=O peak at 1387 cm^{-1} was significantly enhanced in the spectrum of the MFHGs. This result is attributed to the chemical interaction of Co(II), Ni(II) and sulfate ions with the functional groups of the MFHGs.

The thermal properties of the Co(II)- and Ni(II)-adsorbed MFHGs were further investigated by TG-DTA under a N$_2$ atmosphere. The thermal analysis results obtained for the MFHGs after adsorption are shown in Fig. 5b. The residual mass of adsorbed MFHGs was 60.14% at 800 °C and remained almost constant thereafter. The DTA curve of the adsorbed MFHGs can be divided into three significant stages. First, an exotherm was observed at 220 °C because of the evaporation of physically adsorbed water. In the second stage, a broad endotherm appears at approximately 220–320 °C because of the decomposition of bound water molecules inside the material. The third stage shows a wide endotherm beyond 800 °C with an appreciable mass loss, which is mainly attributed to carbonization of the molecular chain of MFHGs, where N, S and O functional groups were totally removed from the MFHGs (He et al., 2018), and adsorbed MFHGs showed a higher weight-loss rate in the third stage. Compared with the MFHGs, the loss in the quality of the material after Co(II) and Ni(II) adsorption slightly increased, but overall, the thermal stability of the material remained acceptable.

Although FTIR is a surface-sensitive technique to observe stretching vibrations of functional groups, they are easily affected by vicinal functional groups. Thus, to further understand the removal mechanism of Co(II) and Ni(II) by MFHGs. The surface elemental compositions of adsorbents were examined by XPS. The wide-scan spectra of adsorbed MFHGs show photoelectron peaks of Fe2p, C1s, O1s, N1s, S2p, Co2p and Ni2p (Fig. 6a); these peaks indicate that Co and Ni were immobilized onto the surface of the MFHGs. The high-resolution spectrum of Co2p (Fig. 6b) shows two peaks at binding energies of 780.76 eV (Co2p 3/2) and 796.5 eV (Co2p 1/2), with a 15.74 eV energy difference between the absolute position of Co2p 3/2 and Co2p 1/2 (Liang et al., 2019), indicating the presence of Co(II) and Co(III). The existence of Co(III) reveals a partial oxidation of Co(II) to Co(III) during the adsorption process. In addition, the same phenomenon of Ni(II) oxidation to Ni(III) was also observed for the Ni(II) adsorbed onto MFHGs (Fig. 6c), as indicated by a large spin-orbit energy separation region of 17.76 eV between Ni2p3/2 and Ni2p1/2 (Sha et al., 2019). Meanwhile, organic groups on the surface of MFHGs may provide electron acceptors for the oxidation of Co and Ni. The XPS C1s spectra (Fig. 6d-e) suggest that some of the following functional groups remained in the adsorbed MFHG matrix: C—C (284.48 eV), C-N(S) (285.18 eV), C—O (286.38 eV) and O-C=O bonds (288.90 eV); the characteristic peaks of C—O (531.38 eV), -OH (531 eV), C-O-C (531.4 eV), -C=O (532.48 eV), FeOx (530.30 eV) and metallic oxides (529.88 eV) (Cui et al., 2016; He et al., 2018) were further confirmed in the O1s spectra (Fig. 6f-g). The binding energy of hydroxyl groups shifted slightly after adsorption, demonstrating that the hydroxyl groups were correlated with the adsorption reaction, in accordance with the results of FTIR. In the Fe2p spectra (Fig. 6h-i), the peaks at 709.4, 711.15, 712.35, 713.74, 719, 724.6 eV are attributed to Fe2p3/2, Fe(II), octahedral Fe(III), tetrahedral Fe(III), Fe(III) and Fe2p1/2, respectively (Dai et al., 2020; Li et al., 2020). These results are consistent with the existence of iron oxides after adsorption. Thus, we speculated that the adsorbed MFHGs would still show strong magnetic recovery performance.

The aforementioned results reveal that at numerous functional groups, crystalline mordenite or amorphous phases remained in the
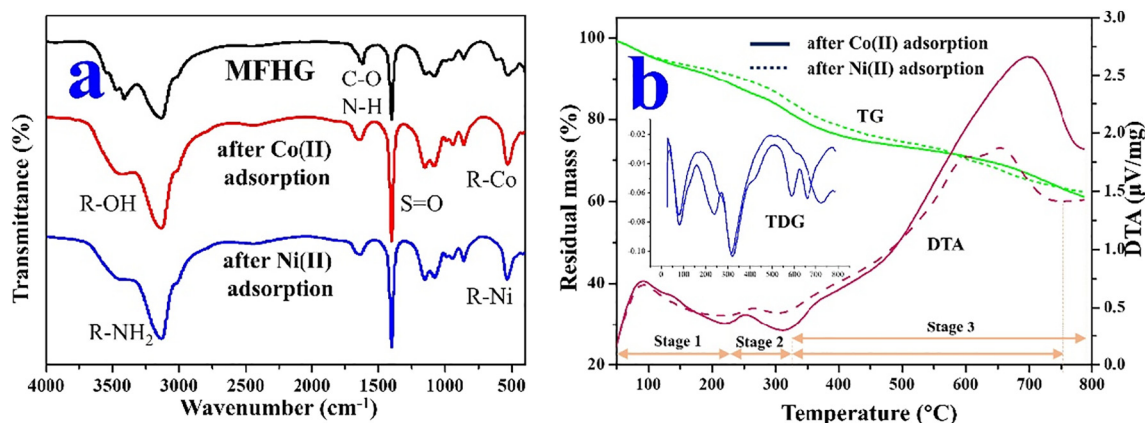

Fig. 5. FTIR spectra of MFHGs before and after adsorption (a), TG-DTA analysis diagram of MFHGs after removal of Co(II) and Ni(II) (b).
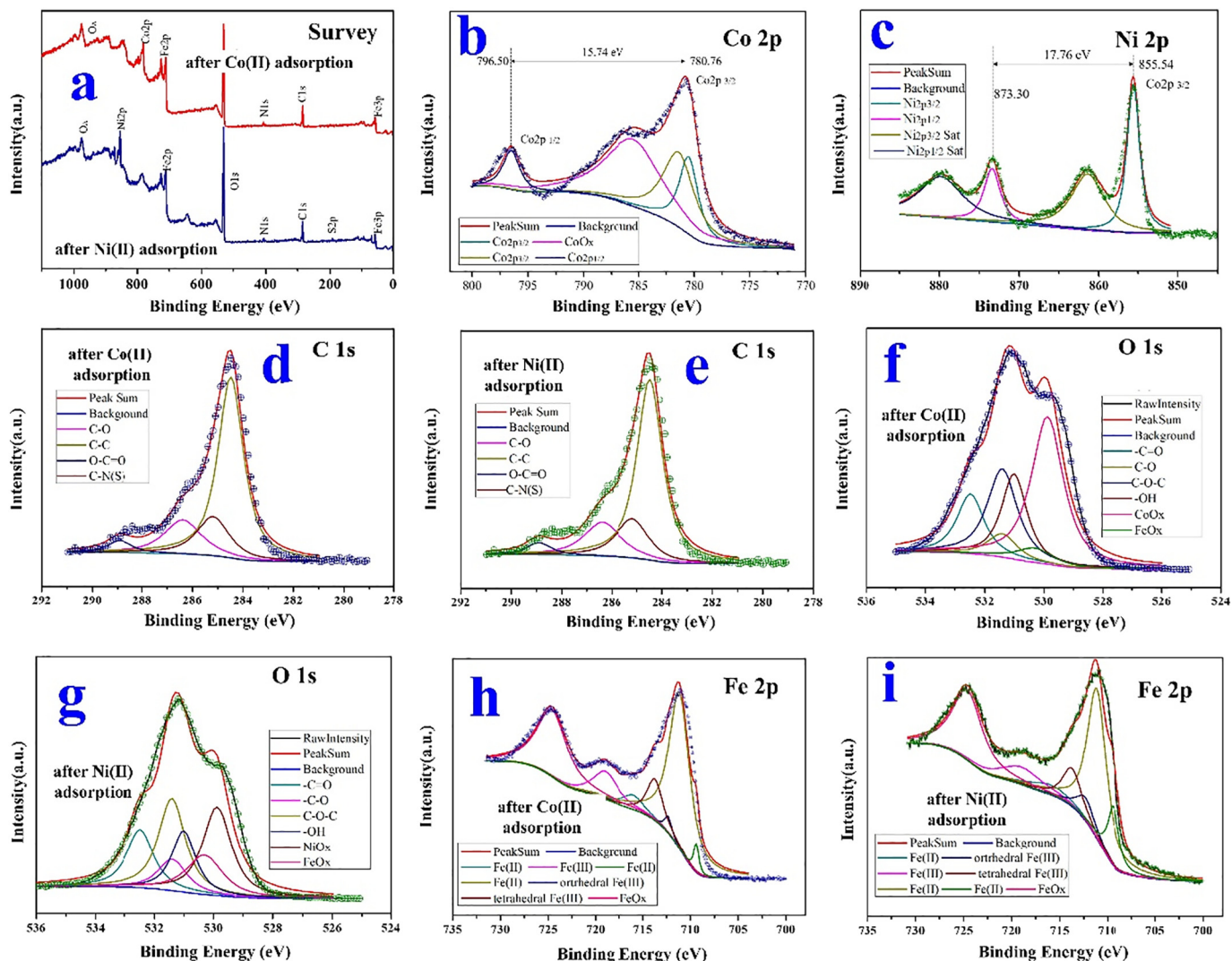
Fig. 6. XPS spectra of MFHGs after Co(II) and Ni(II) removal (a). Co 2p (b), Ni 2p (c), C 1 s (d, e), O 1 s (f, g) and Fe 2p (h, i).

MFHGs after adsorption, which is consistent with the observed intensification of the peaks of organic groups in the FTIR and XPS spectra of MFHGs after adsorption. The XRD patterns of FH, FH/graphene oxide nanofibers, $FeSO_4 \cdot 7H_2O$, MFHGs and the precipitated samples are shown in Fig. S6. All of the characteristic XRD peaks before and after adsorption are mainly observed, with no obvious reflection peaks, except the $FeSO_4 \cdot 7H_2O$ peak. This reveals that FH, FH/graphene oxide nanofibers, and the MFHGs all exist in an amorphous state and exhibit a non-crystalline morphology.

To further ascertain the binding site of the adsorbed Ni and Co complexes, DFT calculations were performed to obtain the energy gaps (ΔE) and stable configurations of the heavy-metal complexes (Sompornpailin et al., 2020). Based on the optimized geometries and the values of ΔE, several reasonable configurations are shown in Table 2. The calculated absolute values of ΔE of CH_3-COO- bonded with Ni(II) (14.34 eV) and Co(II) (14.27 eV) are larger than those of CH_3-CH_2-O-, CH_3-CH_2-S-, CH_3-CH_2-N=, HO-FeO-O- and Fe—O— bonded with Co(II) and Ni(II). These results suggest a stronger binding ability of CH_3-COO-. For these adsorbed Co(II) and Ni(II) cations, no obvious electron cloud overlap was observed, leading to a positive value of their adsorption binding energy. The electron density results confirm the electron transfer or sharing in the adsorption of Co(II) and Ni(II) by the surface functional groups and show that the

cation-exchange chemical adsorption is dominant during the Co(II) and Ni(II) removal process, which is consistent with the results of the isotherm study.

3.5. Regeneration and reuse performance

Regeneration and reuse performance are important factors in measuring the practical application potential of an adsorbent, improving its cost-effectiveness, and reducing operational cost in water treatment applications. The regeneration and reuse performance of MFHGs was evaluated in a newly designed CFRR, and approximately 1 mol/L HCl solution was used as an eluent. The results show that the removal rates of Co(II) and Ni(II) by the MFHGs decreased slightly after six cycles (Fig. S7), and the removal rates of Co(II) and Ni(II) by the MFHGs still reached 72% and 75%, respectively. This result indicates that the MFHGs have high reusability for the removal of Co(II) and Ni(II) in aqueous solution are a low-cost and highly efficient adsorbent for practical applications.

4. Conclusions

In this work, three-dimensional structured MFHGs were prepared by engineering the surface of FH to promote adsorption

Table 2
The HOMO and LUMO distribution of the MFHC residue after adsorption of Co(II) or Ni(II) under different species, as calculated at the SMD/B3LYP/6-31 + G* level of theory. The unit of all the molecular orbital energies is eV.

Ni and Co Chelates	Charge	E_{HOMO} (eV)	E_{LUMO} (eV)	ΔE (eV)
$CH_3\text{-}COO\text{-}Co\text{-}O\text{-}CH_3$	0	-12.052397	2.2181592	14.2705566
$CH_3\text{-}CH_2\text{-}O\text{-}Co\text{-}O\text{-}CH_2\text{-}CH_3$	0	-9.3871779	2.4902592	11.8774371
$CH_3\text{-}COO\text{-}Co\text{-}OOC\text{-}CH_3$	0	-9.145825	1.148262	10.29408
$CH_3\text{-}CH_2\text{-}S\text{-}Co\text{-}O\text{-}CH_2\text{-}CH_3$	0	-7.203303	0.767594	7.970897
$CH_3\text{-}CH_2\text{-}N{=}Co$	1	-7.641384	1.1738394	8.8152237
$OH\text{-}FeO\text{-}O\text{-}Co$	2	-6.810663	0.8701758	7.6808388
$Fe\text{-}O\text{-}Co$	0	-12.00233	2.343053	14.34538
$CH_3\text{-}COO\text{-}Ni\text{-}OOC\text{-}CH_3$	0	-10.66604	2.252443	12.91849
$CH_3\text{-}CH_2\text{-}O\text{-}Ni\text{-}O\text{-}CH_2\text{-}CH_3$	0	-9.153716	1.164860	10.31857
$CH_3\text{-}CH_2\text{-}S\text{-}Ni\text{-}O\text{-}CH_2\text{-}CH_3$	0	-6.872429	0.052243	6.924672
$CH_3\text{-}CH_2\text{-}N{=}Ni$	1	-7.1401761	0.7267791	7.8669552
$HO\text{-}FeO\text{-}O\text{-}Ni$	2	—		

performance toward Co(II) and Ni(II). The results showed that the RSA strategy increased flocculation performance, stability, oxygen-containing functional groups and magnetic recoverability. Moreover, the MFHGs could be activated by volatile acids to realize Co(II) and Ni(II) resource recovery via a novel CFRR. Batch adsorption results revealed that the MFHGs exhibited high sorption capacity for Ni(II) (97.44 mg/g) and Co(II) (104.34 mg/g) at pH 6.0 and 323 K. FTIR, XPS, TG-DTA, and XRD analyses and DFT calculations revealed the chemical interaction of Co(II), Ni(II) and sulfate ions with the hydroxyl groups and amine groups of the MFHGs, and cation-exchange chemical adsorption was dominant in the Co(II) and Ni(II) removal process. Furthermore, the MFHGs exhibited rapid settling capacity, excellent magnetization and large coercivity in high-salt-concentration aqueous solution. Therefore, RSA might be a promising strategy to engineer FH for adsorptive applications, and MFHGs might be an ideal material for water pollution control.

CRediT authorship contribution statement

Runhua Chen: Conceptualization, Methodology. **Yuying Cheng:** Writing - original draft. **Ping Wang:** Supervision. **Qingwei Wang:** Data curation. **Si Wan:** Data curation. **Shunhong Huang:** Methodology. **Rongkui Su:** Writing - review & editing. **Yuxia Song:** Software. **Yangyang Wang:** Writing - review & editing.

Declaration of competing interest

The authors declare that they have no known competing financial interests or personal relationships that could have appeared to influence the work reported in this paper.

Acknowledgements

Appendix A. Supplementary data

Supplementary data to this article can be found online at https://doi.org/10.1016/j.scitotenv.2020.143871.

References

Abbasi, S., Foroutan, R., Esmaeili, H., et al., 2019. Preparation of activated carbon from worn tires for removal of Cu(II), Ni(II) and Co(II) ions from synthetic wastewater. Desalin. Water Treat. 141, 269–278. https://doi.org/10.5004/dwt.2019.23569.

Attar, K., Demey, H., Bouazza, D., et al., 2019. Sorption and desorption studies of Pb(II) and Ni(II) from aqueous solutions by a new composite based on alginate and magadiite materials. Polymers 11 (2), 340. https://doi.org/10.3390/polym11020340.

Awual, M.R., Hasan, M.M., Islam, A., et al., 2020. Optimization of an innovative composited material for effective monitoring and removal of cobalt(II) from wastewater. J. Mol. Liq. 298, 112035. https://doi.org/10.1016/j.molliq.2019.112035.

Badsha, M.A.H., Lo, I.M.C., et al., 2020. An innovative pH-independent magnetically separable hydrogel for the removal of Cu(II) and Ni(II) ions from electroplating wastewater. J. Hazard. Mater. 381, 121000. https://doi.org/10.1016/j.jhazmat.2019.121000.

Bogusz, A., Nowak, K., Stefaniuk, M., et al., 2017. Synthesis of biochar from residues after biogas production with respect to cadmium and nickel removal from wastewater. J. Environ. Manag. 201, 268–276. https://doi.org/10.1016/j.jenvman.2017.06.019.

Cai, W.T., Dionysiou, D.D., Fu, F.L., et al., 2020. CTAB-intercalated molybdenum disulfide nanosheets for enhanced simultaneous removal of Cr(VI) and Ni(II) from aqueous solutions. J. Hazard. Mater. 396, 122728. https://doi.org/10.1016/j.jhazmat.2020.122728.

Cárdenas-González, J.F., Acosta-Rodríguez, I., Téran-Figueroa, Y., et al., 2017. Bioremoval of arsenic (V) from aqueous solutions by chemically modified fungal biomass. Biotech 7 (3), 226. https://doi.org/10.1007/s13205-017-0868-5.

Chaabane, L., Beyou, E., El Ghali, A., et al., 2020. Comparative studies on the adsorption of metal ions from aqueous solutions using various functionalized graphene oxide sheets as supported adsorbents. J. Hazard. Mater. 389, 121839. https://doi.org/10.1016/j.jhazmat.2019.121839.

Chen, Q., Zheng, J., Xu, J., et al., 2019. Insights into sulfamethazine adsorption interfacial interaction mechanism on mesoporous cellulose biochar: coupling DFT/FOT simulations with experiments. Chem. Eng. J. 356, 341–349. https://doi.org/10.1016/j.cej.2018.09.055.

Chen, R.H., Cheng, Y.Y., Wang, P., et al., 2020. High efficient removal and mineralization of Cr(VI) from water by functionalized magnetic fungus nanocomposites. J Cent South Univ 27 (5), 1503–1514. https://doi.org/10.1007/s11771-020-4386-y.

Chen, Q., Tang, Z.Y., Li, H., et al., 2020. An electron-scale comparative study on the adsorption of six divalent heavy metal cations on MnFe2O4@CAC hybrid: experimental and DFT investigations. Chem. Eng. J. 381, 124231. https://doi.org/10.1016/j.cej.2019.122656.

Cui, G.R., Liu, M., Chen, Y., et al., 2016. Synthesis of a ferric hydroxide-coated cellulose nanofiber hybrid for effective removal of phosphate from wastewater. Carbohydr. Polym. 154, 40–47. https://doi.org/10.1016/j.carbpol.2016.08.025.

Dai, L., Li, L., Zhu, W., et al., 2020. Post-engineering of biochar via thermal air treatment for highly efficient promotion of uranium(VI) adsorption. Bioresour. Technol. 298, 122576. https://doi.org/10.1016/j.biortech.2019.122576.

Di Natale, F., Gargiulo, V., Alfe, M., et al., 2020. Adsorption of heavy metals on silica-supported hydrophilic carbonaceous nanoparticles (SHNPs). J. Hazard. Mater. 393, 122374. https://doi.org/10.1016/j.jhazmat.2020.122374.

Fan, H.M., Ma, Y.W., Wan, J.Q., et al., 2020. Adsorption properties and mechanisms of novel biomaterials from banyan aerial roots via simple modification for ciprofloxacin removal. Sci. Total Environ. 708, 134630. https://doi.org/10.1016/j.scitotenv.2019.134630.

Fang, Y., Li, J., Han, P., et al., 2018. Less toxic zinc(ii), diorganotin(iv), gallium(iii) and cadmium(ii) complexes derived from 2-benzoylpyridine N,N-dimethylthiosemicarbazone: synthesis, crystal structures, cytotoxicity and investigations of mechanisms of action. Toxicol. Res. 7, 987–993. https://doi.org/10.1039/C8TX00127H.

Firdaous, L., Fertin, B., Khelissa, O., et al., 2017. Adsorptive removal of polyphenols from an alfalfa white proteins concentrate: adsorbent screening, adsorption kinetics and equilibrium study. Sep. Purif. Technol. 178, 29–39. https://doi.org/10.1016/j.seppur.2017.01.009.

He, S.R., Li, Y.T., Weng, L.P., et al., 2018. Competitive adsorption of Cd^{2+}, Pb^{2+} and Ni^{2+} onto Fe^{3+}-modified argillaceous limestone: influence of pH, ionic strength and natural organic matters. Sci. Total Environ. 637, 69–78. https://doi.org/10.1016/j.scitotenv.2018.04.300.

Hou, T.L., Yan, L.G., Li, J., et al., 2020. Adsorption performance and mechanistic study of heavy metals by facile synthesized magnetic layered double oxide/carbon composite from spent adsorbent. Chem. Eng. J. 384, 123331. https://doi.org/10.1016/j.cej.2019.123331.

Huang, L., Wu, B.C., Wu, Y.J., et al., 2020. Porous and flexible membrane derived from ZIF-8-decorated hyphae for outstanding adsorption of Pb^{2+} ion. J. Colloid Interface Sci. 565, 465–473. https://doi.org/10.1016/j.jcis.2020.01.035.

Jiao, T., Zhao, H., Zhou, J., et al., 2015. Self-assembly reduced graphene oxide nanosheet hydrogel fabrication by anchorage of chitosan/silver and its potential efficient application toward dye degradation for wastewater treatments. ACS Sustain. Chem. & Eng. 3 (12), 3130–3139. https://doi.org/10.1021/acssuschemeng.5b00695.

Jones, M.P., Lawrie, A.C., Huynh, T.T., et al., 2019. Agricultural by-product suitability for the production of chitinous composites and nanofibers utilising Trametes versicolor and Polyporus brumalis mycelial growth. Process Biochem. 80, 95–102. https://doi.org/10.1016/j.procbio.2019.01.018.

Kara, I., Tunc, D., Sayin, F., et al., 2018. Study on the performance of metakaolin based geopolymer for Mn(II) and Co(II) removal. Appl. Clay Sci. 161, 184–193. https://doi.org/10.1016/j.clay.2018.04.027.

Kauling, A.P., Seefeldt, A.T., Pisoni, D.P., et al., 2018. The worldwide graphene flake production. Adv. Mater. 30 (44), 1803784. https://doi.org/10.1002/adma.201803784.

Kumar, A., Sharma, G., Naushad, M., et al., 2020. Bio-inspired and biomaterials-based hybrid photocatalysts for environmental detoxification: a review. Chem. Eng. J. 382, 122937. https://doi.org/10.1016/j.cej.2019.122937.

Lapwanit, S., Trakulsujaritchok, T., Nongkhai, P.N., et al., 2016. Chelating magnetic copolymer composite modified by click reaction for removal of heavy metal ions from aqueous solution. Chem. Eng. J. 289, 286–295. https://doi.org/10.1016/j.cej.2015.12.073.

Lee, K.Y., Kim, K.W., Park, M., et al., 2016. Novel application of nanozeolite for radioactive cesium removal from high-salt wastewater. Water Res. 95, 134–141. https://doi.org/10.1016/j.watres.2016.02.052.

Lei, J., Guo, Q., Yin, D.R., et al., 2019. Bioconcentration and bioassembly of N/S co-doped carbon with excellent stability for supercapacitors. Appl. Surf. Sci. 488, 316–325. https://doi.org/10.1016/j.apsusc.2019.05.136.

Li, J., Fana, M., Li, M., et al., 2020. Cr(VI) removal from groundwater using double surfactant-modified nanoscale zero-valent iron (nZVI): effects of materials in different status. Sci. Total Environ. 717, 137112. https://doi.org/10.1016/j.scitotenv.2020.137112.

Liang, R., Shen, L., Jing, F., et al., 2015. Preparation of MIL-53 (Fe)-reduced graphene oxide nanocomposites by a simple self-assembly strategy for increasing interfacial contact: efficient visible-light photocatalysts. ACS Appl. Mater. & Inter. 7 (18), 9507–9515. https://doi.org/10.1021/acsami.5b00682.

Liang, H.Y., Xiao, K., Wei, L.Y., et al., 2019. Decomplexation removal of Ni(II)-citrate complexes through heterogeneous Fenton-like process using novel CuO-CeO2-CoOx composite nanocatalyst. J. Hazard. Mater. 374, 167–176. https://doi.org/10.1016/j.jhazmat.2019.04.031.

Lin, Z.X., Yuan, P., Yue, Y.Y., et al., 2020. Selective adsorption of co(II)/Mn(II) by zeolites from purified terephthalic acid wastewater containing dissolved aromatic organic compounds and metal ions. Sci. Total Environ. 698, 134287. https://doi.org/10.1016/j.scitotenv.2019.134287.

Liu, X.T., Zhang, X.H., Zhang, K.L., et al., 2016. Sodium persulfate-assisted mechanochemical degradation of tetrabromobisphenol A: efficacy, products and pathway. Chemosphere 150, 551–558. https://doi.org/10.1016/j.chemosphere.2015.08.055.

Liu, X.J., Wu, J.L., Wang, J.L., et al., 2019. Electro-enhanced removal of cobalt ions from aqueous solution by capacitive deionization. Sci. Total Environ. 697, 134144. https://doi.org/10.1016/j.scitotenv.2019.134144.

Meteku, B.E., Huang, J.K., Zeng, J.B., et al., 2020. Magnetic metal-organic framework composites for environmental monitoring and remediation. Coord. Chem. Rev. 413, 213261. https://doi.org/10.1016/j.ccr.2020.213261.

Najafpoor, A., Norouzian-Ostad, R., Alidadi, H., et al., 2020. Effect of magnetic nanoparticles and silver-loaded magnetic nanoparticles on advanced wastewater treatment and disinfection. J. Mol. Liq. 303, 112640. https://doi.org/10.1016/j.molliq.2020.112640.

Panda, L., Rath, S.S., Rao, D.S., et al., 2018. Thorough understanding of the kinetics and mechanism of heavy metal adsorption onto a pyrophyllite mine waste based geopolymer. J. Mol. Liq. 263, 428–441. https://doi.org/10.1016/j.molliq.2018.05.016.

Peres, E.C., Cunha, J.M., Dortzbacher, G.F., et al., 2018. Treatment of leachates containing cobalt by adsorption on Spirulina sp. and activated charcoal. J. Environ. Chem. Eng. 6 (1), 677–685. https://doi.org/10.1016/j.jece.2017.12.060.

Qiu, Y., Xu, X., Xu, Z., et al., 2020. Contribution of different iron species in the iron-biochar composites to sorption and degradation of two dyes with varying properties. Chem. Eng. J. 389, 124471. https://doi.org/10.1016/j.cej.2020.124471.

Rwiza, M.J., Oh, S.Y., Kim, K.W., et al., 2018. Comparative sorption isotherms and removal studies for Pb(II) by physical and thermochemical modification of low-cost agro-wastes from Tanzania. Chemosphere 195, 135–145. https://doi.org/10.1016/j.chemosphere.2017.12.043.

Samuel, M.S., Subramaniyan, V., Bhattacharya, J., et al., 2018. Ultrasonic-assisted synthesis of graphene oxide - fungal hyphae: an efficient and reclaimable adsorbent for chromium(VI) removal from aqueous solution. Ultrason. Sonochem. 48, 412–417. https://doi.org/10.1016/j.ultsonch.2018.06.012.

Sha, L.N., Ye, K., Wang, G., et al., 2019. Rational design of NiCo2S4 nanowire arrays on nickle foam as highly efficient and durable electrocatalysts toward urea electrooxidation. Chem. Eng. J. 359, 1652–1658. https://doi.org/10.1016/j.cej.2018.10.225.

Sierra, J., Roig, N., Papiol, G., et al., 2017. Prediction of the bioavailability of potentially toxic elements in freshwaters. Comparison between speciation models and passive samplers. Sci. Total Environ. 605, 211–218. https://doi.org/10.1016/j.scitotenv.2017.06.136.

Sompornpailin, D., Ratanatawanate, C., Sattayanon, C., et al., 2020. Selective adsorption mechanisms of pharmaceuticals on benzene-1,4-dicarboxylic acid-based MOFs: effects of a flexible framework, adsorptive interactions and the DFT study. Sci. Total Environ. 720, 137449. https://doi.org/10.1016/j.scitotenv.2020.137449.

Velimirovic, M., Auffan, M., Carniato, L., et al., 2018. Effect of field site hydrogeochemical conditions on the corrosion of milled zerovalent iron particles and their dechlorination efficiency. Sci. Total Environ. 618, 1619–1627. https://doi.org/10.1016/j.scitotenv.2017.10.002.

Vithanage, M., Ashiq, A., Ramanayaka, S., et al., 2020. Implications of layered double hydroxides assembled biochar composite in adsorptive removal of contaminants: current status and future perspectives. Sci. Total Environ. 737, 139718. https://doi.org/10.1016/j.scitotenv.2020.139718.

Wang, D.D., Yang, B.W., Ye, Y.X., et al., 2019. Nickel speciation of spent electroless nickel plating effluent along the typical sequential treatment scheme. Sci. Total Environ. 654, 35–42. https://doi.org/10.1016/j.scitotenv.2018.10.389.

Wang, Y.Y., Liu, Y.D., Zhan, W.H., et al., 2020. Stabilization of heavy metal-contaminated soils by biochar: challenges and recommendations. Sci. Total Environ. 729, 139060. https://doi.org/10.1016/j.scitotenv.2020.139060.

Wang, Y.Y., Zheng, K.X., Zhan, W.H., et al., 2021. Highly effective stabilization of Cd and Cu in two different soils and improvement of soil properties by multiple-modified biochar. Ecotox. Environ. Safe. 207, 111294. https://doi.org/10.1016/j.ecoenv.2020.111294.

Yang, X.D., Wan, Y.S., Zheng, Y.L., et al., 2019. Surface functional groups of carbon-based adsorbents and their roles in the removal of heavy metals from aqueous solutions: a critical review. Chem. Eng. J. 366, 608–621. https://doi.org/10.1016/j.cej.2019.02.119.

Yi, Y.Q., Huang, Z.X., Lu, B.Z., et al., 2020. Magnetic biochar for environmental remediation: a review. Bioresour. Technol. 298, 122468. https://doi.org/10.1016/j.biortech.2019.122468.

Yuan, D.H., Zhang, W.J., Cui, J., et al., 2020. Facile fabrication of magnetic phosphorylated chitosan for the removal of Co(II) in water treatment: separation properties and adsorption mechanisms. Environ. Sci. Pollut. Res. 27 (3), 2588–2598. https://doi.org/10.1007/s11356-019-07026-5.

Zare-Dorabei, R., Ferdowsi, S.M., Barzin, A., et al., 2016. Highly efficient simultaneous ultrasonic-assisted adsorption of Pb(II), Cd(II), Ni(II) and Cu (II) ions from aqueous solutions by graphene oxide modified with 2,2′-dipyridylamine: central composite design optimization. Ultrason. Sonochem. 32, 265–276. https://doi.org/10.1016/j.ultsonch.2016.03.020.

Zhang, T.N., He, W., Zheng, H., et al., 2021. Satellite-based ground PM2.5 estimation using a gradient boosting decision tree. Chemosphere, 1288801 https://doi.org/10.1016/j.chemosphere.2020.128801.

Zhang, C.-Z., Yuan, Y., Li, T., et al., 2018. Adsorption and desorption of heavy metals from water using aminoethyl reduced graphene oxide. Environ. Eng. Sci. 35 (9), 978–987. https://doi.org/10.1089/ees.2017.0541.

Zhang, M., Zhang, L., Wang, H., et al., 2020. Hybrid electrocatalytic ozonation treatment of high-salinity organic wastewater using Ni–Ce/OMC particle electrodes. Sci. Total Environ. 724, 138170. https://doi.org/10.1016/j.scitotenv.2020.138170.

Zhao, Y.G., Shen, H.Y., Pan, S.D., et al., 2010. Synthesis, characterization and properties of ethylenediamine-functionalized Fe_3O_4 magnetic polymers for removal of Cr(VI) in wastewater. J. Hazard. Mater. 182 (1), 295–302. https://doi.org/10.1016/j.jhazmat.2010.06.029.

Zhao, L.X., Liang, J.L., Li, N., et al., 2020. Kinetic, thermodynamic and isotherm investigations of Cu^{2+} and Zn^{2+} adsorption on Li-Al hydrotalcite-like compound. Sci. Total Environ. 716, 137120. https://doi.org/10.1016/j.scitotenv.2020.137120.

Zhou, Z.Y., Kong, D.L., Zhu, H.Y., et al., 2018. Preparation and adsorption characteristics of an ion-imprinted polymer for fast removal of Ni(II) ions from aqueous solution. J. Hazard. Mater. 341, 355–364. https://doi.org/10.1016/j.jhazmat.2017.06.010.

Zhu, W., Lei, J., Li, Y., et al., 2019. Procedural growth of fungal hyphae/Fe_3O_4/graphene oxide as ordered-structure composites for water purification. Chem. Eng. J. 355, 777–783. https://doi.org/10.1016/j.cej.2018.08.215.

Zong, L.D., Liu, F.Q., Chen, D., et al., 2018. A novel pyridine based polymer for highly efficient separation of nickel from high-acidity and high-concentration cobalt solutions. Chem. Eng. J. 334, 995–1005. https://doi.org/10.1016/j.cej.2017.10.127.